Forced Advancing & Receding Contact Lines on Soft Solids

Christopher Henkel[1], Vincent Bertin[2], Jacco H. Snoeijer[3], Uwe Thiele[1,4]

[1]Institute of Theoretical Physics, University of Münster, Wilhelm-Klemm-Str. 9, 48149 Münster, Germany.

[2]Université Côte d'Azur, CNRS, INPHYNI UMR 7010, Nice 06200, France.

[3]Physics of Fluids Group, Faculty of Science and Technology, University of Twente, 7500 AE Enschede, The Netherlands.

[4]Center for Data Science and Complexity (CDSC), University of Münster, Correnssstr. 2, 48149 Münster, Germany.

Contributing authors: c_henk08@uni-muenster.de; vincent.bertin@univ-cotedazur.fr; j.h.snoeijer@utwente.nl; u.thiele@uni-muenster.de;

Abstract

We discuss the forced dynamics of an advancing and receding contact line on a soft viscoelastic substrate, using the framework of a mesoscopic thin-film model. Specifically, we consider the geometry of a dip coating experiment where the substrate is dipped into or dragged out of a liquid bath at a prescribed angle and speed. In the receding case, we focus on the forced wetting transition, in which a film is deposited above a critical speed. Numerical continuation reveals the bifurcation scenario and shows how the critical speed is larger on softer substrates. In the advancing case, we show how the viscoelasticity of the substrate gives rise to intricate stick-slip motion in a limited velocity regime.

1 Introduction

The process of replacing an initially dry solid–gas interface by a solid–liquid interface is a central part of many phenomena in interfacial fluid mechanics. Depending on the geometry, the involved materials, and the acting forces, such a process may be relaxational as for spreading drops and the imbibition of a porous medium, or it may be externally driven as in coating technologies and forced wetting experiments [1–3]. Here, we focus on the dip-coating process, in which a solid plate is immersed and/or withdrawn from a bath of simple or complex liquid at a controlled velocity and inclination angle [4–13]. At small withdrawal speed the receding contact line of a partially wetting liquid remains stationary with respect to the surface of the bath while above a critical withdrawal speed this is not the case. Then, the receding contact line will move and a macroscopic liquid film is entrained on the moving substrate. This forced wetting transition is commonly referred to as the Landau–Levich–Derjaguin transition, after the classical theory for viscous film deposition on a withdrawn plate [14–17]. In the asymptotic regime of small capillary number $\mathrm{Ca} = \eta U/\gamma$, the deposited film thickness is controlled by a balance between viscous stresses and capillarity, leading to the characteristic scaling $h_\infty \sim \ell_c \mathrm{Ca}^{2/3}$. Here, η and γ are the dynamic viscosity and surface tension of the liquid, U is the withdrawal velocity, and $\ell_c = \sqrt{\gamma/\rho g}$ is the capillary length (g is the gravitational acceleration and ρ is the mass density of the liquid).

Beyond its fundamental relevance, dip coating is of considerable practical importance. It provides a robust route for producing liquid layers of controlled thickness, depositing surfactants or particles, and fabricating molecular films on solid substrates. Closely related protocols form the basis of Langmuir–Blodgett transfer, where monolayers assembled at the free surface of a liquid bath are transferred onto moving solid supports [18–23]. The same basic hydrodynamic mechanism also underlies a broad class of coating and printing technologies, for which control over the onset of film entrainment is essential [4, 24].

A central question for receding contact lines is to understand the critical speed at which a film is deposited. For rigid substrates, this forced-wetting problem has been studied extensively using lubrication theory, asymptotic analysis, numerical continuation, and direct numerical time simulations. These studies have shown that the transition from a steady meniscus to a deposited film is governed by the interplay between viscous bending of the free surface, capillary pressure, gravity, and microscopic contact-line physics [1–3, 24]. In particular, bifurcation analyses clarify how the structure, stability, and existence range of steady meniscus states depend on the withdrawal velocity and inclination angle of the plate, and furthermore characterize various qualitative transitions connecting, e.g., the onset of film deposition to the occurrence of a saddle-node bifurcation in the family of meniscus states [5–8, 25–27]. Complementary, asymptotic approaches are employed to derive scaling laws for the critical capillary number at which steady receding contact-line states cease to exist [28–30].

Most theoretical descriptions of Landau–Levich transfer assume that the solid support is perfectly smooth and rigid [10]. However, many substrates encountered in experiments and applications are elastically or viscoelastically compliant, i.e., adapt to the moving contact line [31]. Soft gels, elastomers, biological tissues, polymer coatings, and swollen hydrogel layers and polymer brushes can deform appreciably under capillary forces and viscous stresses [32–35]. The wetting of such materials is now understood to be qualitatively different from wetting on rigid solids, because the liquid contact line exerts a localized capillary traction that produces an elastocapillary ridge in the substrate [36, 37]. The resulting deformation modifies the apparent contact angle, the dissipation near the moving contact line, and the relation between microscopic and macroscopic wetting dynamics [32, 34]. In addition, viscoelastic dissipation in the substrate can lead to contact-line braking, velocity-dependent wetting forces, stick–slip motion, and other dynamical effects that are absent for ideally rigid solids [38–41].

In this paper we revisit the Landau–Levich forced-wetting transition for a compliant substrate. To isolate the essential elastohydrodynamic coupling, the substrate is represented by a linear Winkler foundation, for which the local vertical displacement is proportional to the normal stress exerted by the liquid. Although simplified, this model captures the leading effect of substrate compliance while retaining a tractable long-wave formulation. Related local-foundation descriptions have been widely used in soft-lubrication and elastohydrodynamic problems, where they provide a minimal framework for coupling viscous flow to elastic deformation [42]. In the case of a receding contact line, i.e., when extracting a plate from a bath, our objective is to determine how substrate softness alters the bifurcation structure of the dip-coating problem, the critical withdrawal speed for film entrainment, and the morphology of the meniscus near onset. For the advancing contact line, i.e., when immersing the plate into the bath, we aim at identifying parameter regions where the contact line does not advance steadily but in a jerky manner – the so-called stick-slip motion of the contact line.

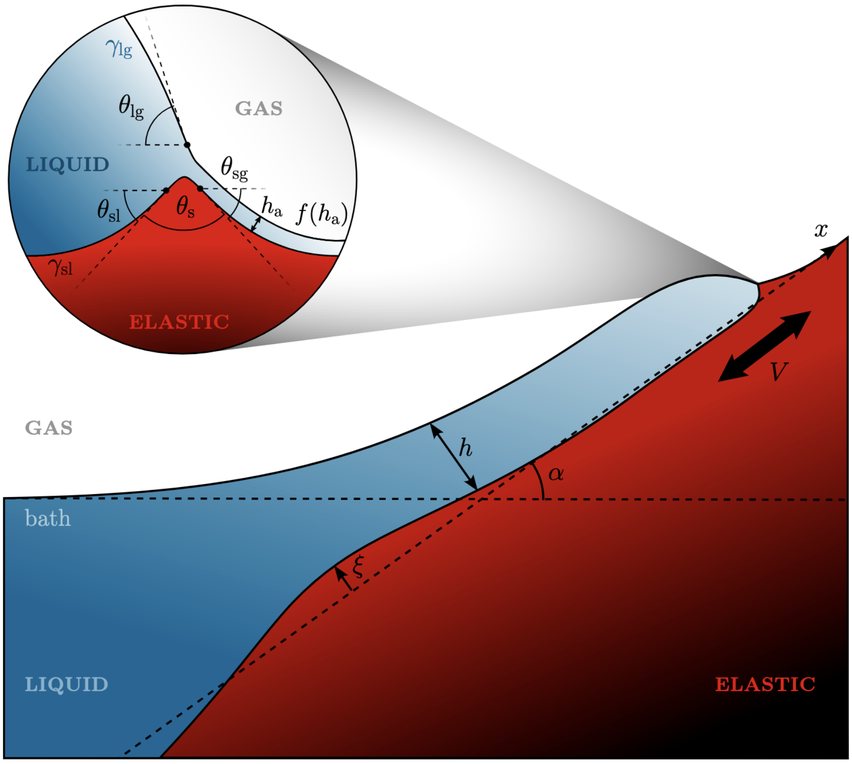

Fig. 1 Cross section of a Landau-Levich meniscus with a foot being dragged out. The local thickness of the liquid (blue) perpendicular to the undeformed substrate plane is given by the scalar function $h(x,t)$ while the deformation of the soft substrate (red) is described by a function $\xi(x,t)$. The elastic substrate is pulled out of or immersed into the bath with a velocity V and is inclined w.r.t. the gravity equipotential by an angle α. The inset shows a zoom of the Neumann contact line region where the liquid-gas interface meets the substrate surface. In the mesoscopic picture a meniscus with finite contact angle coexists with an adsorption layer of height $h_{\rm a}$ that covers the solid-gas interface as described by a corresponding wetting potential $f(h)$. The contact line becomes a contact line region and the angles are defined at the inflection points of the interfaces.

2 Modeling

2.1 Governing equations

Consider a system as depicted in Fig. 1. A viscoelastic substrate (red area) is pulled out of or pushed into a liquid bath (blue area) at velocity V and inclination angle α. The coordinate system is oriented such that the $y=0$ plane is aligned with the substrate surface, i.e., its undeformed reference configuration, and the x-coordinate points up-hill. The substrate is considered soft such that it is deformed by the pressure exerted by the liquid. The local liquid layer thickness and substrate profile are then described by the scalar functions $h(x,t)$ and $\xi(x,t)$, respectively. The three-phase contact line, where the liquid-gas interface meets the substrate surface, is characterized by the formation of a wetting ridge and is in a static scenario described by Neumann's laws. Assuming the contact-angles in the Neumann region as well as the plate inclination angle to be small, the liquid dynamics can be described by the thin-film equation [43]

$$\partial_t h = \frac{\partial}{\partial x}\left[\frac{h^3}{3\eta}\frac{\partial p_h}{\partial x}\right] - V\partial_x h \ , \qquad (1)$$

while for the substrate we employ a compressible Kelvin-Voigt dynamics paired with a Winkler foundation model as in Ref. [44],

$$\partial_t \xi = -\frac{1}{\zeta}p_\xi - V\partial_x \xi \ . \qquad (2)$$

The motion of the plate is modeled by the convection term added to both equations where the sign is chosen such that for $V > 0$ the plate moves in positive x-direction, i.e., the substrate is pulled out of the bath, see Fig. 1. Here, we introduced the dynamic viscosity of the liquid η, and an elastic friction constant ζ describing the dissipation inside the elastic layer. The coupled kinetic equations (1) and (2) correspond to a conserved and nonconserved dynamics, respectively [45] as the liquid is incompressible [46] and the soft substrate is assumed to be fully compressible [44]. The dynamics is driven by the substrate velocity V that keeps the system permanently out of equilibrium. However, if the substrate remains at rest, the model is of gradient dynamics form and the system ultimately approaches an equilibrium state [47].

Correspondingly, the pressures p_h and p_ξ at the respective interfaces follow as functional variations of a governing free energy $\mathcal{F}$ which is decomposed as follows

$$\mathcal{F}[h,\xi] = \mathcal{F}_{\mathrm{cap}}[h,\xi] + \mathcal{F}_{\mathrm{wet}}[h] + \mathcal{F}_{\mathrm{el}}[\xi] + \mathcal{F}_{\mathrm{g}}[h,\xi]. \tag{3}$$

The first term corresponds to capillary energy of both the solid-liquid and the liquid-gas interfaces. In the long-wave limit it is given by

$$\mathcal{F}_{\mathrm{cap}}[h,\xi] = \int_{\mathbb{R}} \left[\frac{\gamma_{\mathrm{lg}}}{2}(\partial_x h + \partial_x \xi)^2 + \frac{\gamma_{\mathrm{sl}}}{2}(\partial_x \xi)^2\right] \mathrm{d}x, \tag{4}$$

where γ_{lg} and γ_{sl} are the liquid-gas and solid-liquid interfacial energies, respectively. To allow for contact line movement we employ an adsorption layer model by introducing a wetting potential $f(h)$ of the form [45]

$$f(h) = \frac{A}{2h^2}\left[\frac{2}{5}\left(\frac{h_{\mathrm{a}}}{h}\right)^3 - 1\right], \tag{5}$$

that combines attractive long-range van der Waals interactions and repulsive short-range adhesion forces [24, 47, 48]. This wetting potential ensures that the substrate is always covered by an ultrathin adsorption layer of thickness h_{a} where it is considered macroscopically dry [49]. Consider the zoom in Fig. 1 for a visualization of how the contact line region changes when going to the mesoscopic description. The Hamaker constant A is chosen such that the effective solid-gas interface energy $\gamma_{\mathrm{sg}} = \gamma_{\mathrm{sl}} + \gamma_{\mathrm{lg}} + f(h_{\mathrm{a}})$ is recovered. It is thus related to the equilibrium contact angle θ_{Y} through Young's law, $\gamma_{\mathrm{sg}} - \gamma_{\mathrm{sl}} = \gamma_{\mathrm{lg}}\cos\theta_{\mathrm{Y}}$, which yields

$$A = \frac{10}{3}\gamma h_{\mathrm{a}}^2(1-\cos\theta_{\mathrm{Y}}) \sim \frac{5}{3}\gamma\theta_{\mathrm{Y}}^2 h_{\mathrm{a}}^2, \tag{6}$$

where the long-wave approximation has been applied in the last step. The contribution of the wetting potential to the complete free energy functional is

$$\mathcal{F}_{\mathrm{wet}}[h] = \int_{\mathbb{R}} f(h)\mathrm{d}x. \tag{7}$$

Next, the work stored in the elastic deformation of the substrate is taken into account. In the simple case of the Winkler foundation model, with only vertical displacement being considered, this contribution is given by a quadratic potential [50]

$$\mathcal{F}_{\mathrm{el}}[\xi] = \int_{\mathbb{R}} \frac{\xi^2}{2S}\mathrm{d}x, \tag{8}$$

i.e., as for a simple continuous spring, with effective softness, or inverse stiffness, S. Finally, the contribution of gravitation is accounted via the potential

$$\begin{aligned}\mathcal{F}_{\mathrm{g}}[h,\xi] &= \int_{\mathbb{R}} \left[\frac{\rho g\cos\alpha}{2}((h+\xi)^2 - \xi^2) + \rho g \sin\alpha h x\right] \mathrm{d}x \\ &\sim \int_{\mathbb{R}} \left[\frac{\rho g}{2}((h+\xi)^2 - \xi^2) + \rho g \alpha h x\right] \mathrm{d}x,\end{aligned} \tag{9}$$

where ρ is the liquid mass density and g the gravitational acceleration. The pressures then follow as variations w.r.t. the two variables

$$p_h = \frac{\delta\mathcal{F}}{\delta h} = -\gamma_{\mathrm{lg}}\partial_x^2(h+\xi) - \Pi(h) + \rho g\left[h + \xi + x\alpha\right], \tag{10}$$

$$p_\xi = \frac{\delta\mathcal{F}}{\delta \xi} = -\gamma_{\mathrm{lg}}\partial_x^2(h+\xi) - \gamma_{\mathrm{sl}}\partial_x^2\xi + \frac{\xi}{S} + \rho g h, \tag{11}$$

where we introduce the disjoining pressure $\Pi(h) = -\partial_h f(h)$.

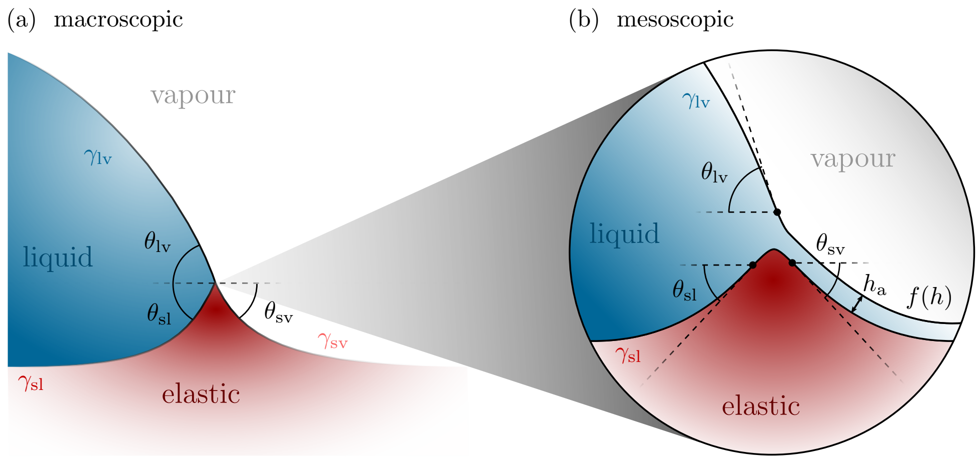

Fig. 2 Sketch of a Neumann contact line region as created by a liquid-gas interface hitting the surface of an elastic substrate. In the macroscopic picture (a) the interfaces meet at the three phase contact angles at the respective angles θ_{lg}, θ_{sl} and θ_{sg}. In the mesoscopic picture (b) the solid-gas interface is covered by an adsorption layer of height h_{a} and the corresponding energy corrected via a wetting potential $f(h)$. The contact line becomes a contact region and the angles are defined by the deflection points of the interfaces.

2.2 Macroscopic nondimensionalization

The resulting equations are nondimensionalized using the capillary length $\ell_{\mathrm{cap}} = \sqrt{\gamma_{\mathrm{lg}}/(\rho g)}$ as horizontal and $\theta_{\mathrm{Y}}\ell_{\mathrm{cap}}$ as vertical scale (as in [29])

$$h \to \theta_{\mathrm{Y}}\ell_{\mathrm{cap}}\bar{h}, \quad \xi \to \theta_{\mathrm{Y}}\ell_{\mathrm{cap}}\bar{\xi}, \quad x \to \ell_{\mathrm{cap}}\bar{x}\ . \tag{12}$$

The characteristic time scale is chosen as $\frac{\eta\ell_{\mathrm{cap}}}{\gamma_{\mathrm{lg}}\theta_{\mathrm{Y}}^3}$, while the pressure scale is $\gamma_{\mathrm{lg}}\theta_{\mathrm{Y}}/\ell_{\mathrm{cap}}$. Then, the dimensionless dynamical system (bar quantities are dimensionless) reads

$$\partial_{\bar{t}}\bar{h} = \partial_{\bar{x}}\left(\frac{\bar{h}^3}{3}\partial_{\bar{x}}\bar{p}_h\right) - \mathrm{Ca}\ \partial_{\bar{x}}\bar{h}\ , \tag{13}$$

$$\partial_{\bar{t}}\bar{\xi} = -\frac{1}{\mathcal{T}}\bar{p}_{\xi} - \mathrm{Ca}\ \partial_{\bar{x}}\bar{\xi} \tag{14}$$

and the pressures

$$\bar{p}_h = -\partial_{\bar{x}}^2(\bar{h}+\bar{\xi}) - \frac{5}{3}\epsilon^2\Pi(\bar{h}) + (\bar{h}+\bar{\xi}) + \bar{x}\varphi \tag{15}$$

$$\bar{p}_{\xi} = -\partial_{\bar{x}}^2(\bar{h}+\bar{\xi}) - \sigma\partial_{\bar{x}}^2\bar{\xi} + \frac{\bar{\xi}}{\mathcal{L}} + \bar{h} \tag{16}$$

with

$$\mathrm{Ca} = \frac{\eta V}{\gamma_{\mathrm{lg}}\theta_{\mathrm{Y}}^3}\ , \qquad \mathcal{T} = \frac{\zeta\ell_{\mathrm{cap}}\theta_{\mathrm{Y}}^3}{\eta}\ , \qquad \varphi = \frac{\alpha}{\theta_{\mathrm{Y}}}\ ,$$
$$\epsilon = \frac{h_{\mathrm{a}}}{\theta_{\mathrm{Y}}\ell_{\mathrm{cap}}}\ , \qquad \sigma = \frac{\gamma_{\mathrm{sl}}}{\gamma_{\mathrm{lg}}}\ ,$$
$$\mathcal{L} = \frac{\gamma_{\mathrm{lg}}S}{\ell_{\mathrm{cap}}^2} = \rho g S = \left(\frac{\ell_{\mathrm{ec}}}{\ell_{\mathrm{cap}}}\right)^2 \tag{17}$$

Here we have defined the elastocapillary length as $\ell_{\mathrm{ec}} = \sqrt{\gamma_{\mathrm{lg}}S}$. This nondimensionalization will be used in Sec. 3.

2.3 Mesoscopic nondimensionalization

Alternatively, a nondimensionalization that is adapted to the mesoscopic description can be used. The latter is relevant when contact-line physics is mainly governed by the local microscopic structure, and will be employed in Sec. 4. The mesoscopic scaling chooses the adsorption layer height h_{a} as characteristic scale for all vertical lengths instead of the capillary length in the macroscopic scaling. The horizontal scales are renormalized such that the disjoining pressure and capillary term are of same order, i.e., horizontal scales are renormalized by $h_{\mathrm{a}}\sqrt{3/5}/\theta_{\mathrm{Y}}$

$$h \to h_{\mathrm{a}}\tilde{h}\ , \quad \xi \to h_{\mathrm{a}}\tilde{\xi}\ , \quad x \to \sqrt{\frac{3}{5}}\frac{h_{\mathrm{a}}\tilde{x}}{\theta_{\mathrm{Y}}} \tag{18}$$

The characteristic time scale is chosen accordingly as $\left(\frac{3}{5}\right)^2 \frac{3\eta h_{\mathrm{a}}}{\gamma_{\mathrm{lg}}\theta_{\mathrm{Y}}^4}$ and pressure scale as $\frac{5}{3}\frac{\gamma_{\mathrm{lg}}\theta_{\mathrm{Y}}^2}{h_a}$. Then, the dimensionless dynamical system (here tilde quantities are dimensionless) reads

$$\partial_{\tilde{t}}\tilde{h} = \partial_{\tilde{x}}\left(\tilde{h}^3\partial_{\tilde{x}}\tilde{p}_h\right) - \left(\frac{3}{5}\right)^{\frac{3}{2}} 3\mathrm{Ca}\partial_{\tilde{x}}\tilde{h}\ , \tag{19}$$

$$\partial_{\tilde{t}}\tilde{\xi} = -\frac{1}{\tau}\tilde{p}_\xi - \left(\frac{3}{5}\right)^{\frac{3}{2}} 3\mathrm{Ca}\partial_{\tilde{x}}\tilde{\xi} \tag{20}$$

and the pressures

$$\tilde{p}_h = -\partial_{\tilde{x}}^2(\tilde{h}+\tilde{\xi}) - \Pi(\tilde{h}) + \frac{3}{5}\epsilon^2\left(\tilde{h}+\tilde{\xi}+\tilde{x}\varphi\sqrt{\frac{3}{5}}\right)\ , \tag{21}$$

$$\tilde{p}_\xi = -\partial_{\tilde{x}}^2(\tilde{h}+\tilde{\xi}) - \sigma\partial_{\tilde{x}}^2\tilde{\xi} + \frac{\tilde{\xi}}{s} + \frac{3}{5}\epsilon^2\tilde{h} \tag{22}$$

with

$$\tau = \frac{5}{3}\frac{\theta_{\mathrm{Y}}^2}{3}\frac{\zeta h_{\mathrm{a}}}{\eta} = \frac{5}{9}\epsilon\mathcal{T}, \qquad s = \frac{5}{3}\frac{\gamma_{\mathrm{lg}}\theta_{\mathrm{Y}}^2}{h_{\mathrm{a}}^2}S = \frac{5}{3}\frac{\mathcal{L}}{\epsilon^2}\ . \tag{23}$$

This nondimensionalization will be used in Sec. 4.

2.4 Numerical methods

In the following we explore the behavior of receding and advancing contact lines by numerically solving Eqs. (13) and (14) using two different open source software frameworks. AUTO-07P [51] is a `Fortran`-based software package for numerical continuation and bifurcation analysis. It is used to perform the parameter continuation for the receding contact line case, presented in Sec. 3.2. The remaining results are produced using PYOOMPH [52]; a `Python` package for finite-element simulations and bifurcation analysis, based on the `C++` libraries OOMPH-LIB [53, 54] and GiNaC [55]. It is used to perform both, time simulations as well as parameter continuation. Such continuation techniques follow a branch of states when a parameter, e.g., the capillary number Ca, is changed [56, 57] and are frequently used in the analysis of mesoscopic hydrodynamic models [26, 43, 45, 58, 59].

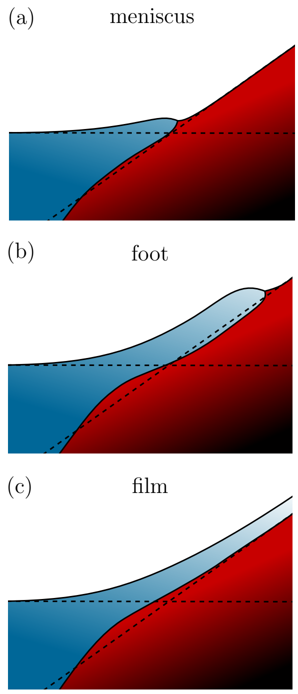

Fig. 3 Scenarios occurring in the case of a receding contact line (Ca>0). These are (a) a steady meniscus, (b) a meniscus with a steady or stationary advancing foot, and a meniscus coexisting with a macroscopic film that is dragged out of the bath.

3 Receding contact line Ca > 0

In case of a receding contact line, that is the substrate is pulled out of the bath, a great variety of scenarios may occur depending on the inclination angle and pulling velocity. These scenarios are extensively studied for perfectly rigid substrates in Ref. [26]. In general there are three scenarios to be distinguished: (1) the meniscus remains steady and is only slightly deformed in dragging direction [Fig. 3 (a)], (2) a finite liquid foot is pulled out of the bath [Fig. 3 (b)], the length of which is governed by a balance of the viscous drag and the downhill gravitational pull, and (c) an ever growing liquid foot which results in a homogeneous film deposited on the substrate [Fig. 3 (c)]. In industrial applications such a deposition of a homogeneous liquid layer is the desired or an unwanted outcome, depending on the context. It is therefore important to predict the critical plate velocity V_c for deposition. This critical velocity marks the threshold at which the static meniscus destabilizes into an ever growing liquid foot that is dragged along the substrate.

In the following, we study this wetting transition for elastic substrates (i.e. we set the substrate relaxation time $\mathcal{T} = 0$). The steady states are traced by a numerical continuation method, based on which we identify the critical plate velocity. Specifically, we are interested in identifying how this critical speed depends on the softness of the substrate. In this section we stick to the macroscopic nondimensionalization as introduced in Sec. 2.2.

3.1 Steady-state equation & boundary conditions

The dynamic wetting transition occurs via destabilization of the steady meniscus state. This state is determined by solving the static equations, i.e., Eqs. (1) and (2) with $\partial_t h = \partial_t \xi = 0$. The liquid equation can then be integrated once, leading to

$$\partial_{\bar{x}}^3(\bar{h}+\bar{\xi}) = 3\mathrm{Ca}\frac{\bar{h}_\infty - \bar{h}}{\bar{h}^3} + \partial_{\bar{x}}(\bar{h}+\bar{\xi}) + \varphi \tag{24}$$

$$- \epsilon\partial_{\bar{h}}\Pi(\bar{h})\partial_{\bar{x}}\bar{h} \; , \tag{25}$$

$$\partial_{\bar{x}}^2\bar{\xi} = \frac{1}{\sigma}\left[\frac{\bar{\xi}}{\mathcal{L}} + \bar{h} + \mathcal{T}\mathrm{Ca}\;\partial_{\bar{x}}\bar{\xi} - \partial_{\bar{x}}^2(\bar{h}+\bar{\xi})\right] \; . \tag{26}$$

where the integration constant $\bar{h}_\infty$ corresponds to the normalized liquid flux. Below a critical capillary number, no macroscopic liquid film is entrained; only the residual flux associated with the mesoscopic adsorption layer remains, so that $h_\infty = h_\mathrm{a}$. Above a critical capillary number Ca_c, a macroscopic film with $h_\infty \gg h_\mathrm{a}$ is entrained.

On the far left, i.e., $x \to -\infty$ in Fig. 1, the liquid-gas interface transitions into the bath surface and is assumed perfectly horizontal, that is

$$\lim_{\bar{x}\to-\infty}\partial_{\bar{x}}(\bar{h}+\bar{\xi}) = -\varphi \tag{27}$$

in the rotated coordinate system. Due to vanishing curvature of the liquid-gas interface in the bath, the substrate height is governed exclusively by the balance of gravitational pressure exerted by the liquid and elastic restoring forces

$$\bar{\xi} = -\mathcal{L}\bar{h} \tag{28}$$

which leads to the condition

$$\lim_{\bar{x}\to-\infty}\partial_{\bar{x}}\bar{\xi} = \frac{\varphi\mathcal{L}}{1-\mathcal{L}} \; . \tag{29}$$

Note, that this restricts us to the parameter range $0 \leq \mathcal{L} < 1$ where for $\mathcal{L} \to 1$ the depression of the substrate due to gravity, i.e., the weight of the liquid, becomes equal to the liquid layer thickness such that $\bar{\xi} \to -\bar{h}$ and $\bar{h}+\bar{\xi} \to 0$. Finally, in the out-of-bath direction, i.e., $x \to \infty$ in Fig. 1, we have $h \to h_\infty$. Both, $\bar{h}$ and $\bar{\xi}$, are assumed to exhibit vanishing curvature such that Eq. (28) remains valid, which leads to the boundary conditions

$$\lim_{\bar{x}\to\infty}\bar{h} = \epsilon \; , \tag{30}$$

$$\lim_{\bar{x}\to\infty}\bar{\xi} = -\mathcal{L}\epsilon. \tag{31}$$

3.2 Bifurcation diagrams: Critical speed versus softness

Using continuation techniques, Eqs. (25) and (26) are solved numerically while some parameter, e.g., Ca, is changed, allowing us to follow the branch of steady menisci in parameter space. The resulting bifurcation diagram is shown in Fig. 4(a) for different values of the substrate softness $\mathcal{L}$. When increasing Ca from zero, eventually each branch folds back at a saddle-node bifurcation where the state becomes unstable. These bifurcations define the critical capillary number Ca_c, i.e., a critical substrate velocity, beyond which there exist no steady meniscus states anymore. The main interest of this section is to establish how Ca_c depends on the softness. Figure 4(b) reports this critical capillary number as a function of $\mathcal{L}$. The rigid case corresponds to $\mathcal{L} = 0$, and one observes a monotonic increase of Ca_c as the substrate becomes softer.

To quantify how the critical speed increases with softness, we propose the following mechanism. In the rigid limit, the critical speed crucially depends on the separation of a microscopic and a macroscopic scale. The macroscopic scale is set by the capillary length ℓ_cap in the dip-coating geometry. In the present mesoscopic model, this microscopic scale is provided by the adsorption thickness h_a, which regularizes the contact-line region through the disjoining pressure. Thus, h_a is a mesoscopic parameter of the hydrodynamic

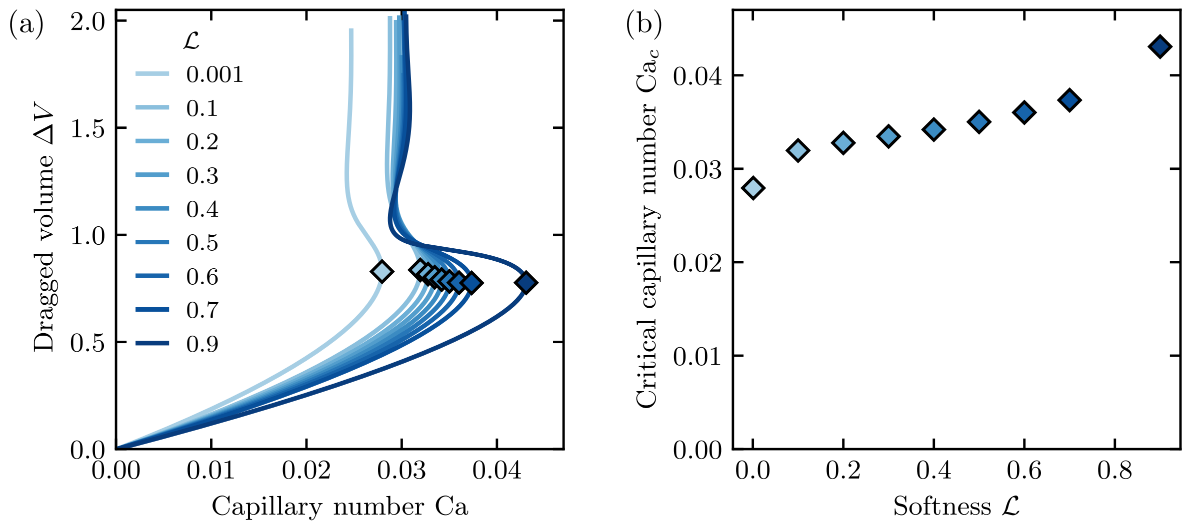

Fig. 4 Bifurcation diagrams showing the branch of steady meniscus states, characterized by the dragged-out volume ΔV against the capillary number Ca, i.e., the dimensionless velocity of the substrate, for different softness $\mathcal{L}$ of the substrate ranging from very rigid $\mathcal{L} = 0.001$ to very soft $\mathcal{L} = 0.9$. A clear trend is visible in the shift of the branches as the softness increases. The critical capillary number Ca_c, where the dynamic wetting transition occurs, is marked by diamonds and shown in (b) versus the softness parameter $\mathcal{L}$. The dimensionless adsorption layer thickness is fixed to $\epsilon = 0.001$, while $\sigma = 1$.

model, but it plays the role of the microscopic cut-off in the asymptotic argument.

The larger the scale separation between microscale and macroscale, the more dissipation is encountered during contact line motion; by consequence, the maximum speed decreases with increased scale separation. We argue that the introduction of the elastocapillary length ℓ_{ec}, related to the substrate deformation, provides a new cut-off scale for the viscous stress. Indeed, substrate deformation becomes significant when $\ell_{\mathrm{ec}} > h_{\mathrm{a}}$. This increase in microscopic cut-off scale is expected to lead to a reduced dissipation, thereby increasing the critical speed of the forced wetting transition.

To test the above hypothesis, we explore the dependence of Ca_c on the ratio $h_{\mathrm{a}}/(\theta\ell_{\mathrm{cap}})$, which is the relevant parameter in the rigid limit, and on the ratio $\ell_{\mathrm{ec}}/(h_{\mathrm{a}}/\theta)$. The result is shown in Fig. 5, where the colors indicate different $h_{\mathrm{a}}/(\theta\ell_{\mathrm{cap}})$. On the left panel, the respective lowest data points correspond to the rigid substrate. The black dashed line corresponds to the rigid asymptotic theory of Ref. [29] for the critical point of the transition. Specifically, the critical capillary number Ca_c is the solution of the implicit equation

$$0 = 1 - 9\mathrm{Ca}_c \ln\left(k_1 \frac{\ell_{\mathrm{cap}}\mathrm{Ca}_c^{1/3}\theta_Y}{h_{\mathrm{a}}\alpha}\right), \quad k_1 = 0.187. \tag{32}$$

We remark that Ref. [29] uses a Navier slip model to regularize the contact line singularity, while an adsorption layer is used here. Therefore, here we replaced the slip length used in Ref. [29] by the adsorption layer thickness, and the numerical prefactor k_1 inside the logarithm in Eq. (32) has been fitted on the numerical data of the most rigid case. We observe the numerical data to converge to (32) for smaller ratios $h_{\mathrm{a}}/(\theta_Y\ell_{\mathrm{cap}})$, i.e., when the scale separation is larger, in line with the asymptotic nature of the theory. The right panel of Fig. 5 shows the dependence on softness, via $\ell_{\mathrm{ec}}/(h_{\mathrm{a}}/\theta)$. As the elastocapillary length becomes larger than h_{a}/θ_Y, the critical speed gradually increases. Indeed, this is in line with a reduction of dissipation due to ℓ_{ec} serving at the microscopic cutoff. More quantitatively, the dependence on elastocapillary length is relatively weak, and seems to follow a $\propto \ln \ell_{\mathrm{ec}}$ scaling in the soft limit. Based on this observation, we propose an

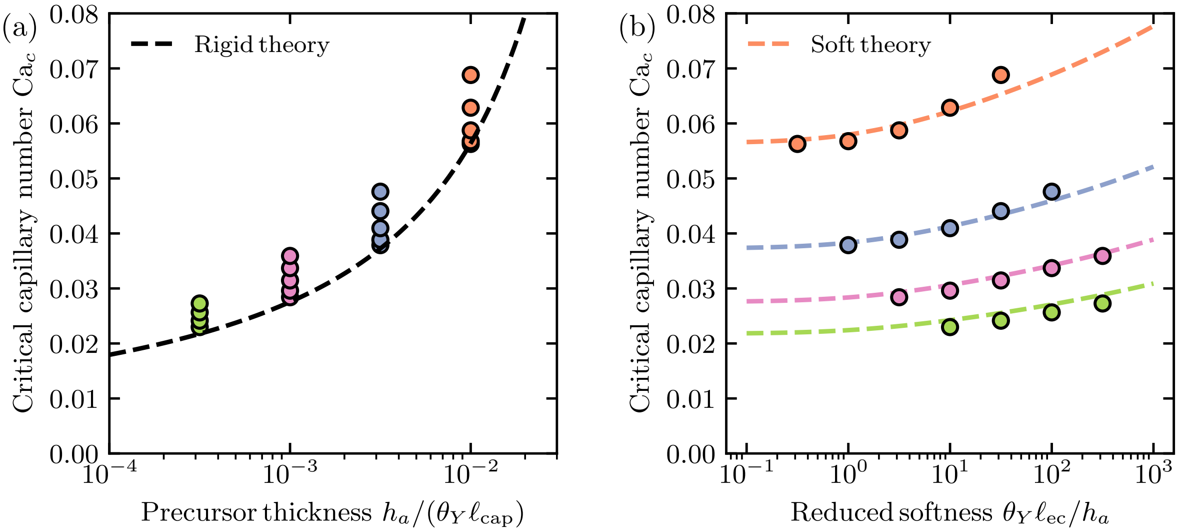

Fig. 5 Critical capillary number $\mathrm{Ca_c}$ as a function of (a) scaled adsorption layer thickness $h_\mathrm{a}/(\theta_\mathrm{Y}\ell_\mathrm{cap})$ and (b) softness parameter $\theta_Y\ell_\mathrm{ec}/h_\mathrm{a} = \sqrt{\mathcal{L}}/\epsilon$. The markers of different color in (a) indicate different adsorption layer thickness to capillary length ratio. With increasing scale separation the agreement of the numerically determined critical capillary number with the one predicted by Eggers [29] improves. For given scale separation (color) $\mathrm{Ca_c}$ increases with the softness, i.e., the lowest marker refers to a rigid substrate. As the softness increases a higher capillary number has to be reached to drag out a film. The dependence is roughly captured by the fit corresponding to Eq. (33).

interpolation function as

$$
\begin{aligned}
0 =& 1 - 9\mathrm{Ca_c} \ln\left(k_1 \frac{\ell_\mathrm{cap}\mathrm{Ca}_c^{1/3}\theta_Y}{h_\mathrm{a}\alpha}\right) \\
&\times \left(1 - k_2 \ln\left(1 + \frac{\theta_Y \ell_\mathrm{ec}}{h_\mathrm{a}}\right)\right), \quad k_2 = 0.045,
\end{aligned} \tag{33}
$$

where the numerical prefactor k_2 has been fitted globally on all data of Fig. 5. The fit indeed suggests the emergence of a softness-induced regime that might be amenable to asymptotic analysis, in the spirit of the rigid theory [60].

We conclude this section by illustrating the dynamics above the critical point, i.e., when no steady state exists, using time-resolved numerical simulations. This is illustrated in Figure 6 by a space-time plot where the left panel focuses on the liquid interface and shows the continuous deposition of a film, while the right panel highlights the corresponding elastic deformation of the substrate. These simulations correspond to a plate velocity just above the critical value. These results confirm that the bifurcation of the steady states in Fig. 4 is indeed associated to the onset of film formation, where the contact line gradually progresses up the plate, once the critical speed is exceeded.

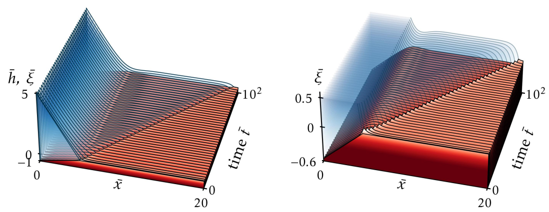

Fig. 6 Space-time plot of the profiles of the (left) free surface of the liquid and the (right) soft substrate for a continuously growing liquid foot that is pulled out of the bath when increasing the capillary number to a value $\mathrm{Ca} = 0.095$ slightly above the critical value $\mathrm{Ca_c}$. The remaining parameters are $\mathcal{L} = 0.1$, $\epsilon = 0.01$, $\sigma = 1$, $\mathcal{T} = 0$ and $\varphi = 1$.

4 Advancing contact line $\mathrm{Ca} < 0$

4.1 Stick-slip behavior

When immersing the considered soft substrate into the liquid ($V < 0$), a phenomenon occurs at the now advancing three-phase contact line that is not observed when extracting the substrate from the bath, i.e., for a receding contact line. Namely, there exist parameter ranges where the contact line does not advance steadily but in a jerky manner.

Such stick-slip motion is common for advancing and receding contact lines on real, i.e., topographically and chemically heterogeneous substrates where the contact line seldom proceeds smoothly but instead moves through a sequence of pinning and depinning events [1, 61–66]. Then, a finite force is needed for depinning – an effect closely related to contact angle hysteresis on random substrates [67, 68]. Investigations for regularly patterned substrates [69–74] allow for deeper insights into the details of the mechanism and resulting bifurcation structure. During the stick phase, the contact line is anchored at a heterogeneity while the contact angle evolves quasi-statically; once a critical angle is exceeded, the contact line rapidly slips to a new metastable configuration.

Besides the mentioned cases where the stick-slip motion is caused by the interaction of the contact line with preexisting substrate heterogeneities, stick-slip dynamics may also emerge for ideally homogeneous substrates that only become nonuniform in the presence of three-phase contact. However, then additional degrees of freedom need to be involved that interact with the moving contact line in such a way that a self-organized stick-slip dynamics emerges. A prominent example is the deposition of regular or irregular patterns of a solute at a receding contact line of a solution or suspension with a volatile solvent - the so called coffee-stain effect [75–81]. More recently, stick-slip behavior was also reported for contact lines moving on adaptive and flexible substrates. Experimental observations exist for forced or driven wetting (expanding droplets) on polymer brushes [82, 83] and on soft solid substrates like viscoelastic gels [39, 84–87] and polymer films [88]. The behavior is also reproduced within a number of modeling approaches [40, 41, 89]. For reviews see [34, 90]. Note that for the adaptive brush-covered substrate stick-slip is reported for advancing contact lines [40, 82] while for soft solids it is found in the advancing case [39, 41, 84, 86, 87] and in the receding case [85].

As for the advancing contact line in the Landau-Levich geometry a macroscopically dry substrate is immersed into the liquid, there is no

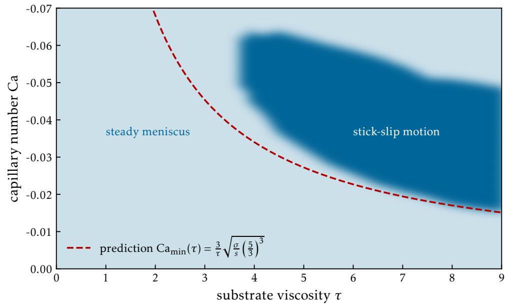

Fig. 7 Occurrence of stick-slip motion in the (Ca, τ)-plane. The light blue area indicates parameter ranges where the steady meniscus state is linearly stable. It is unstable in the dark blue region where time-simulations show stick-slip behavior. The red dashed line represents the prediction of the onset of the stick-slip regime as deduced in the main text [Eq. (41)]. In the numerical simulations stick-slip is only found above a critical substrate friction constant, here $\tau \approx 3.5$. The remaining parameters are $\sigma = 0.1$, $s = 10^2$.

macroscopic liquid film where downhill gravity and uphill dragging force balance. Therefore, in the following investigation of stick-slip motion, for simplicity, we neglect gravity, i.e., we employ the model presented in section (2.1) without $\mathcal{F}_{\mathrm{g}}$.

In the receding situation, a precise description of the outer scale is essential, as it governs the transition between the scenarios of wetting (see Fig. 3, meniscus-foot-film). By contrast, the stick-slip instability discussed here is not controlled by this outer structure. Rather, it is a local instability of the advancing contact line coupled to the substrate deformation. In this sense, the wetting ridge plays the role of a self-generated heterogeneity. Its characteristic size is set by the elastocapillary length ℓ_{ec}, whereas the gravity-controlled outer scale ℓ_{cap} is not expected to affect the mechanism to leading order. For this reason, in the following investigation of stick-slip motion, we neglect gravity and employ the model presented in Sec. 2 without the gravitational contribution $\mathcal{F}_{\mathrm{g}}$. In this limit, the gravity-based parameter ϵ, defined in Sec. 2.2, is no longer a control parameter. Instead, the relevant softness is measured by the mesoscopic parameter $s = \frac{5}{3}\frac{\mathcal{L}}{\epsilon^2} = 5\ell_{\mathrm{ec}}^2/(3h_a^2)$, which compares the elastocapillary length to the adsorption-layer scale. Equivalently, the relevant non-dimensional parameter characterizing the substrate friction is τ. Hence, the nondimensionalization of Sec. 2.3 will be used in the remainder of the paper.

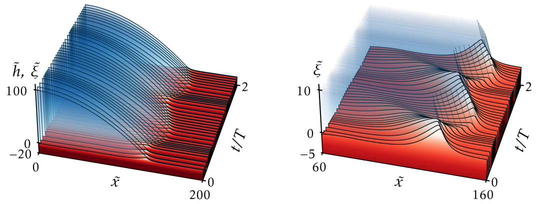

Fig. 8 Space-time plot of the profiles of the (left) free surface of the liquid and the (right) soft substrate illustrating the typical dynamic behavior of the three-phase contact line and the wetting ridge in the stick-slip regime, namely, at $\tau = 5$ and $\mathrm{Ca} = -0.043$. The remaining parameters are as in Fig. 7.

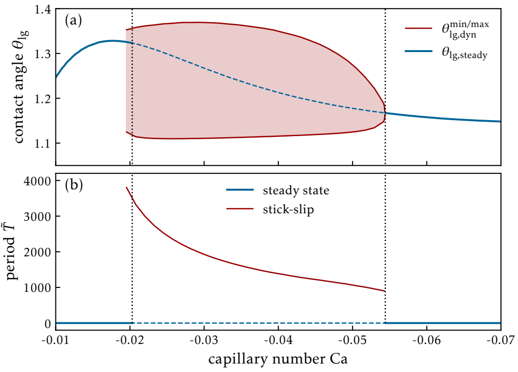

Fig. 9 (a) Dynamic liquid-gas contact angles θ_{lg}, obtained by extrapolating the steady-state numerical interface profiles to the contact-line region, are shown as a function of the capillary number Ca. Linearly stable and unstable steady menisci are indicated by solid and dashed blue lines, respectively. For the time-periodic stick-slip states, the minimum and maximum values of θ_{lg} during one oscillation cycle are shown as red lines. The small range of Ca where both states are linearly stable indicates a narrow hysteresis region at the lower end of the stick-slip regime. (b) Time period $\tilde{T}$ (in mesoscopic time units) of the stick-slip motion. The remaining parameters are as in Fig. 7.

Here, we combine numerical continuation of steady meniscus profiles with direct time simulations. The continuation provides the steady states and their linear stability in the parameter plane spanned by the nondimensional immersion velocity $\mathrm{Ca} < 0$ and the substrate friction constant τ. Direct time simulations are then used to characterize the corresponding unsteady dynamics. In the linearly unstable region, the long-time behavior of the system corresponds to regular time-periodic stick-slip motion. A typical example, taken near the center of the stick-slip region, is shown as a space-time plot in Fig. 8.

The stability results are summarized in Fig. 7. There, stick-slip motion of the contact line occurs in the dark blue region while in the light blue region the steady meniscus is linearly stable. Overall, we find that below a lower critical substrate friction constant, here $\tau \approx 3.5$, the steady meniscus is stable for all plate velocities while above this critical value an intermediate velocity range exists where regular stick-slip motion prevails at large times. As in the case of a polymer brush-covered substrate [40], also here we do not observe more complex spatio-temporal states than time-periodic states.

To further analyze the onset and properties of the stick-slip motion, we present in Fig. 9(a) the dynamic angle θ_{ij}, with ij the corresponding phases, as a function of the Capillary number for a fixed τ. Here, we define a dynamic angle as the angle formed by an interface ij with the reference $y = 0$ undeformed substrate, obtained by extrapolating the numerical steady profiles. Fig. 9(b) furthermore provides the time-period $\tilde{T}$. Inspecting the figure, we note that θ_{lg} has a non-monotonic evolution with $|\mathrm{Ca}|$, meaning that it becomes larger with increasing $|\mathrm{Ca}|$ at small $|\mathrm{Ca}|$, but decreases at larger $|\mathrm{Ca}|$. The Capillary number where the dynamic angle is locally maximal roughly coincides with the lower end of the range where stick-slip is found.

Overall, the behavior is similar to observations reported in [40] for a contact line advancing on an adaptive substrate formed by a polymer brush that can absorb liquid and swell. In particular, the behavior at the lower end of the stick-slip region is qualitatively nearly equivalent. However, at the upper end of the stick-slip region, in [40] the angle θ_{lg} increases again while here it continues to slowly decrease with increasing $|\mathrm{Ca}|$. It only starts to increase again at much larger $|\mathrm{Ca}|$, namely for the parameters of Fig. 9 at about $\mathrm{Ca}{=}-0.088$ (cf. Fig. 10).

For an adaptive polymer-brush substrate that can deform under absorption of liquid, [40] provides estimates for the lower and upper limits of the stick-slip velocity regime based on a time scale argument and a Gibbs condition, respectively. Next, we investigate whether these estimates can be employed also in the present case.

4.2 Low-velocity onset of stick-slip motion

The lower velocity limit of the stick-slip regime is determined by the competition of two time scales. The first, τ_r, characterizes the relaxation of the viscoelastic substrate in response to an external force. Here, it is proportional to the Kelvin–Voigt time scale corresponding to the product of substrate friction constant with softness, i.e. ζS. The second, τ_v, is the time required for the contact line to travel a distance comparable to the width of the wetting ridge at the imposed velocity. Stick-slip motion is expected to set in when both time scales become comparable, $\tau_r \simeq \tau_v$. Below this threshold the liquid forms a static meniscus with a fully developed wetting ridge, whereas above it the substrate can no longer relax fast enough to follow the moving contact line.

Both time scales can be made explicit by solving the substrate dynamics induced by an upward-pulling point force, as detailed in Appendix A. Using the mesoscopic nondimensionalization, the solution reads

$$\tilde{\xi}(\tilde{x},\tilde{t}) \;=\; \frac{1}{2}\int_0^{\tilde{t}} \frac{\exp\left(-\dfrac{\tilde{x}^2\tau}{4\sigma\tilde{t}'}-\dfrac{\tilde{t}'}{\tau s}\right)}{\sqrt{\pi\sigma\tau\,\tilde{t}'}}\,\mathrm{d}\tilde{t}' \,. \tag{34}$$

For $\tilde{t}\to\infty$ the substrate profile converges towards the ridge-like shape

$$\tilde{\xi}_\infty(\tilde{x}) \;=\; \lim_{\tilde{t}\to\infty}\tilde{\xi}(\tilde{x},\tilde{t}) \;=\; \frac{1}{2}\sqrt{\frac{s}{\sigma}}\exp\left(-\frac{|\tilde{x}|}{\sqrt{\sigma s}}\right)\,, \tag{35}$$

which is characterized by the vertical length scale $\tilde{\xi}_r = \tilde{\xi}_\infty(0) = \frac{1}{2}\sqrt{s/\sigma}$ and the horizontal length scale $\tilde{\ell}_r = 2\sqrt{\sigma s}$. The resulting ridge profile is shown in Fig. 11 in Appendix A.

The horizontal extent $\tilde{\ell}_r$ fixes the travel time scale. Since in the mesoscopic nondimensionalization the advection term is scaled by $(3/5)^{3/2}3\mathrm{Ca}$, this expression plays the role of the dimensionless contact-line velocity, the time to traverse one ridge width is

$$\tilde{\tau}_v \;=\; \sqrt{\left(\frac{5}{3}\right)^3}\,\frac{\tilde{\ell}_r}{3\mathrm{Ca}} \;=\; \sqrt{\left(\frac{5}{3}\right)^3}\,\frac{2\sqrt{\sigma s}}{3\mathrm{Ca}}\,. \tag{36}$$

The relaxation time scale $\tilde{\tau}_r$ follows from the temporal build-up of the ridge tip at $\tilde{x}=0$ (i.e., Eq. (38) for $\tilde{x}=0$)

$$\tilde{\xi}(0,\tilde{t}) \;=\; \frac{1}{2}\int_0^{\tilde{t}}\frac{e^{-\tilde{t}'/\tau s}}{\sqrt{\pi\sigma\tau\,\tilde{t}'}}\,\mathrm{d}\tilde{t}'\,, \tag{37}$$

which, using the substitution $\tilde{t}'=\tau s\,u^2$, evaluates to

$$\begin{aligned}\tilde{\xi}(0,\tilde{t}) \;&=\; \frac{1}{2}\sqrt{\frac{s}{\sigma}}\,\frac{2}{\sqrt{\pi}}\int_0^{\sqrt{\tilde{t}/\tau s}} e^{-u^2}\,\mathrm{d}u \\ &=\; \tilde{\xi}_r\,\mathrm{erf}\left(\sqrt{\frac{\tilde{t}}{\tau s}}\right)\,,\end{aligned} \tag{38}$$

with the Gauss error function $\mathrm{erf}(\cdot)$. The resulting prediction for the tip dynamics is compared with numerical simulations in Fig. 12 in Appendix A.

A natural measure of the relaxation is the half-value time, at which the tip has reached half of its asymptotic height,

$$\tilde{\tau}_{1/2} \;=\; \tau s\left[\mathrm{erf}^{-1}\left(\tfrac{1}{2}\right)\right]^2 \;\approx\; \frac{\tau s\,\ln 2}{3.047}\,, \tag{39}$$

so that the relaxation time scale is

$$\tilde{\tau}_r \;=\; \frac{\tau s}{3.047}\,. \tag{40}$$

Equating the two time scales, $\tilde{\tau}_v=\tilde{\tau}_r$, finally yields an estimate of the lower velocity bound of the stick-slip regime,

$$\tilde{\tau}_v=\tilde{\tau}_r \quad\Rightarrow\quad \mathrm{Ca}_{\min} \;\approx\; \frac{6.1}{3\tau}\sqrt{\frac{\sigma}{s}\left(\frac{5}{3}\right)^3}\,. \tag{41}$$

In Figure 7 the estimate is indicated by a red dashed line. A comparison with the results of the linear stability analysis of the steady meniscus state show very good agreement at large substrate friction constant τ and an increasing deviation at smaller τ. The lower critical τ is not captured by the estimate.

4.3 High-velocity limit

For an adaptive polymer-brush substrate that can deform under absorption of liquid, Ref. [40, 90] shows that the high-velocity cessation of stick-slip motion is well captured by a simple Gibbs

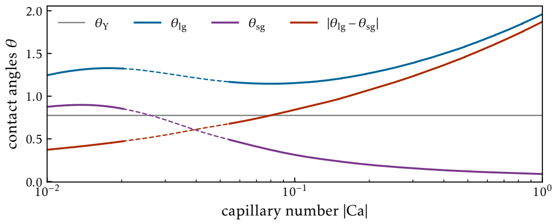

Fig. 10 Dynamic liquid-gas (θ_{lg}, blue) and solid-gas (θ_{sg}, purple) contact angles, extracted from the steady-state numerical profiles, are shown as functions of the capillary number Ca < 0. In the range indicated by dashed lines, time simulations converge to stick-slip motion. Furthermore, the angle difference $|\theta_{\mathrm{lg}} - \theta_{\mathrm{sg}}|$ (red) is compared to the equilibrium Young angle θ_Y (gray). This allows an assessment of the Gibbs criterion. All parameters are as in Fig. 9. Here, the mesoscopic nondimensionalization is used, for which the Young angle corresponds to $\theta = \sqrt{3/5}$ (solid gray line).

criterion that predicts the depinning of a static contact line from sharp corners of a topographically structured solid rigid substrate when control parameters like liquid volume are changed [91, 92]. It has also been successfully applied in other out-of-equilibrium situations [93].

In our case, the condition limits the slope of the liquid–gas interface encoded in the dynamic angle θ_{lg} (shown in Fig. 9) relative to the maximal angle of the outer flank of the wetting ridge, here θ_{sg}. The criterion states that if the difference $|\theta_{\mathrm{lg}} - \theta_{\mathrm{sg}}|$ is larger than the equilibrium Young angle θ_{Y} the contact line is in an unstable state and will depin.

Fig. 10 shows the relevant dynamic angles, and as well their difference in comparison with the the static Young angle for a larger range of Ca than Fig. 9. Inspection of the figure shows that the dynamic angle θ_{lg} increases with increasing substrate speed at small and large |Ca|, however, decreases at intermediate values. In contrast, θ_{sg} only increases at small |Ca| and then continuously decreases. The resulting difference $|\theta_{\mathrm{lg}} - \theta_{\mathrm{sg}}|$ increases monotonically.

The dynamic Gibbs condition corresponds to the statement that the contact line will detach from the tip of the wetting ridge once the opening between the two interfaces can no longer even temporarily sustain the equilibrium (Young) configuration at the tip,

$$\theta_{\mathrm{lg}}(\mathrm{Ca}) - \theta_{\mathrm{sg}}(\mathrm{Ca}) \;\geq\; \theta_{\mathrm{Y}} \;, \tag{42}$$

i.e., when in Fig. 10 $|\theta_{\mathrm{lg}} - \theta_{\mathrm{sg}}|$ crosses the static Young angle θ_{Y} at Ca ≈ -0.09. Then, the contact line begins to *surf* the ridge, terminating the stick-slip regime.

As for the case of an advancing contact line on a polymer brush [40], stick-slip cycles occur only over a subset of the velocity interval where θ_{lg} decreases. Comparing the observed stick-slip region with the theoretical predictions, we find that the low-velocity boundary is well approximated by both, the onset of the decreasing-θ_{lg} regime and the cross-over of time scales, whereas the high-velocity boundary is predicted by the Gibbs criterion that coincides with the end of the decreasing-θ_{lg} regime. The agreement is better at the low-velocity boundary than at the high-velocity boundary. At the parameter values of Fig. 10 the larger difference is about 25%.

We conclude that in the high-velocity limit, a dynamic Gibbs condition provides the correct order of magnitude for the cessation of stick-slip motion, but is not precise enough to provide a quantitative prediction.

5 Conclusion

We have investigated the driven (de)wetting on compliant substrates, namely, the forced dynamics of advancing and receding contact lines on soft elastic substrates in a Landau-Levich geometry. This provides a minimal yet rich setting in which the interplay of capillarity, wettability, substrate softness and driving force can be studied systematically within a mesoscopic hydrodynamic framework. In particular, numerical continuation allowed us to characterize stable and unstable steady menisci while direct time simulations have provided information regarding the complex unsteady dynamics.

For receding contact lines, our main result is that the critical capillary number for the forced wetting transition increases with the softness of the substrate. Thus, softer substrates can sustain larger withdrawal speeds before a macroscopic Landau-Levich film is deposited. Hence, the influence of deformation is already present even in the absence of explicit dissipation or friction in the substrate. It is therefore not only the viscoelastic loss in the solid that modifies the transition, but also the static elastic deformation of the substrate in the contact line region and the resulting change in the contact-line geometry [60]. The formation of an elastic wetting ridge alters the local matching between the microscopic contact-line region and the outer meniscus. This effectively delays the onset of film deposition, as quantified by an increase of the critical Capillary number with substrate softness. We interpret this trend as a consequence of the elastocapillary length reducing the effective scale separation that controls contact-line dissipation. This picture motivates an interpolation formula that reproduces the observed dependence on softness. However, a complete asymptotic description is considerably more involved. In particular, in the viscocapillary regime the governing equations contain cubic nonlinearities that lead to a nontrivial structure of the asymptotic solutions and make a direct analytical treatment challenging.

For advancing contact lines, the viscoelastic response of the substrate gives rise to the qualitatively different phenomenon of stick-slip motion that occurs for sufficiently soft substrates in an intermediate range of driving velocities. In this regime, the contact line alternates between phases of very slow motion, during which the wetting ridge builds up and pins the contact line, and rapid slip events, during which the contact line depins from the ridge and advances to a new position. Such dynamics only occur when the substrate relaxation is sufficiently slow, corresponding to a minimum value of the substrate friction parameter. If the substrate relaxes too rapidly, the wetting ridge can follow the contact line quasi-statically and no pronounced stick-slip instability is observed. The period of the stick-slip cycle decreases with increasing driving velocity, consistent with the reduced time available for the substrate to deform during each cycle. At the low-velocity onset, the transition to stick-slip motion shows hysteresis, indicating the coexistence of steady sliding and time-periodic states over a finite parameter range. This onset can be rationalized by comparing two characteristic time scales: the time associated with the imposed contact-line motion and the intrinsic relaxation time of the substrate. When these become comparable, the substrate can no longer adjust adiabatically, enabling oscillatory dynamics. This fully agrees with results obtained of an adaptive polymer-brush substrate that can deform under absorption of liquid [40, 90].

In contrast, the high-velocity cessation of stick-slip motion is not very well captured by a dynamic Gibbs criterion that, however, works well in the case of the polymer-brush substrate [40]. This suggests that the disappearance of oscillations at large velocities is governed by the full dynamic coupling between liquid interface and substrate deformation rather than by a purely local geometric criterion.

The numerical treatment of these problems remains demanding because of the strong separation of length and time scales. The contact-line region, the wetting ridge, the outer meniscus and the bath scale all have to be resolved simultaneously, while in the unsteady advancing case the rapid slip events coexist with much slower substrate relaxation. Continuation techniques are therefore essential, but their application is technically challenging. A natural next step would be to continue the Hopf bifurcation curves that mark the destabilization of the steady meniscus state in two-parameter space in order to obtain a complete phase diagram for the onset and disappearance of stick-slip motion. Similarly, the continuation of time-periodic states and of their bifurcations is complicated by the need to discretize the temporal domain, where uniform resolution is inefficient because the dynamics are strongly localized in time during slip events.

Overall, the present results demonstrate that soft substrates can fundamentally alter both the steady and unsteady dynamics of forced wetting, and highlight several open analytical and numerical challenges for future work.

Data Availability

The data that support the findings of this study as well as the python codes for creating the figures will be made publicly available and deposited on an online depository.

Acknowledgments

We acknowledge financial support from NWO through the VICI Grant No. 680-47-632 and from Deutsche Forschungsgemeinschaft (DFG) under Project No. 422913191 within SPP2171 for SN1451-2.

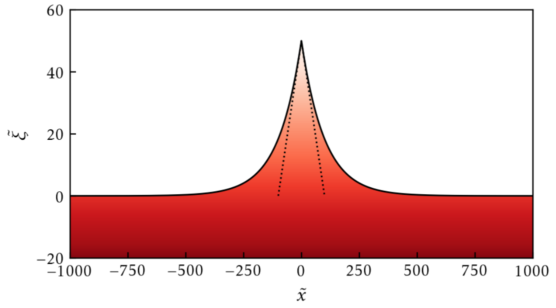

Fig. 11 Stationary shape of the wetting ridge forming in response to a vertical point force, Eq. (44). The exponential decay sets the ridge width $\tilde{\ell}_r = 2\sqrt{\sigma s}$, which forms the base of the triangular envelope (dashed). The parameters are $s = 10^{-4}$ and $\sigma = 1$.

A Wetting ridge relaxation

We consider the dynamics of the viscoelastic substrate in response to a suddenly applied, upward-pulling point force $\alpha(\tilde{x}, \tilde{t}) = \delta(\tilde{x})\Theta(\tilde{t})$, where $\Theta(\tilde{t})$ denotes the Heaviside step function. Such a force triggers the build-up of a (wetting) ridge, whose final, stationary shape is governed by the static equation

$$0 \;=\; \sigma\,\partial_{\tilde{x}}^2\tilde{\xi}(\tilde{x}) - \frac{\tilde{\xi}(\tilde{x})}{s} + \delta(\tilde{x})\,. \tag{43}$$

This linear equation is solved by decaying exponential functions, yielding

$$\tilde{\xi}_\infty(\tilde{x}) \;=\; \lim_{\tilde{t}\to\infty}\tilde{\xi}(\tilde{x},\tilde{t}) \;=\; \frac{1}{2}\sqrt{\frac{s}{\sigma}}\,e^{-\frac{|\tilde{x}|}{\sqrt{\sigma s}}}\,. \tag{44}$$

The corresponding stationary ridge profile is shown in Fig. 11. It has a cusped tip at $\tilde{x} = 0$ and decays exponentially over the horizontal length scale $\sqrt{\sigma s}$; the ridge width $\tilde{\ell}_r = 2\sqrt{\sigma s}$ sets the base of the triangular envelope indicated in the figure.

The transient relaxation towards this shape obeys the diffusion-type equation

$$\tau\,\partial_{\tilde{t}}\tilde{\xi}(\tilde{x},\tilde{t}) \;=\; \sigma\,\partial_{\tilde{x}}^2\tilde{\xi}(\tilde{x},\tilde{t}) - \frac{\tilde{\xi}(\tilde{x},\tilde{t})}{s} + \delta(\tilde{x})\Theta(\tilde{t})\,. \tag{45}$$

A Fourier transformation in space reduces this to an inhomogeneous, first-order ordinary differential equation in time for each wavenumber $\tilde{k}$,

$$\tau\,\partial_{\tilde{t}}\tilde{\xi}(\tilde{k},\tilde{t}) \;=\; -\sigma\tilde{k}^2\tilde{\xi}(\tilde{k},\tilde{t}) - \frac{\tilde{\xi}(\tilde{k},\tilde{t})}{s} + \frac{\Theta(\tilde{t})}{\sqrt{2\pi}}\,,$$

which is solved directly to give

$$\tilde{\xi}(\tilde{k},\tilde{t}) \;=\; A(\tilde{k})\left[1 - e^{-\lambda(\tilde{k})\tilde{t}}\right]\,, \tag{46}$$

$$\text{with}\quad A(\tilde{k}) \;=\; \frac{1}{\sqrt{2\pi}}\frac{s}{\sigma s\tilde{k}^2 + 1}$$

$$\text{and}\quad \lambda(\tilde{k}) \;=\; \frac{1}{\tau\sqrt{2\pi}}\frac{1}{A(\tilde{k})}\,.$$

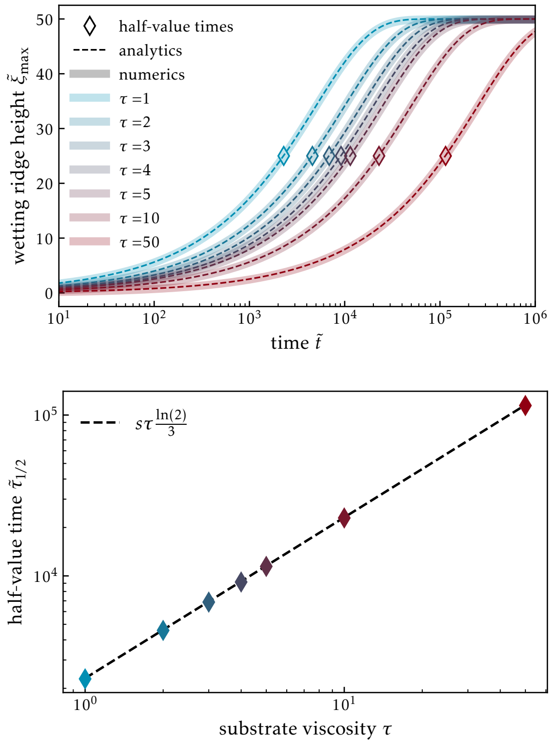

Fig. 12 (top) Build-up of the ridge tip $\tilde{\xi}(0,\tilde{t})$ for different effective substrate viscosities τ: analytical prediction Eq. (38) (dashed lines) versus numerical simulations (thick lines), showing excellent agreement. The half-value times $\tilde{\tau}_{1/2}$ are indicated by diamonds. (bottom) Half-value times obtained from the simulations (diamonds) compared with the analytical estimate Eq. (40) (black dashed line) as a function of τ, displayed on a log–log scale. Remaining parameters are $s = 10^{-4}$ and $\sigma = 0.1$

The amplitude $A(\tilde{k}) = \lim_{\tilde{t}\to\infty}\tilde{\xi}(\tilde{k},\tilde{t}) = \tilde{\xi}_\infty(\tilde{k})$ is precisely the Fourier transform of the static solution (44), while $\lambda(\tilde{k})$ is the associated, $\tilde{k}$-dependent relaxation rate. Expressing $A(\tilde{k})$ in terms of $\lambda(\tilde{k})$ allows the solution to be written as a time integral,

$$\begin{aligned}\tilde{\xi}(\tilde{k},\tilde{t}) &= \frac{1}{\tau\sqrt{2\pi}}\frac{1}{\lambda(\tilde{k})}\left[1-e^{-\lambda(\tilde{k})\tilde{t}}\right] \\ &= \frac{1}{\tau\sqrt{2\pi}}\int_0^{\tilde{t}} e^{-\lambda(\tilde{k})\tilde{t}'}\,\mathrm{d}\tilde{t}' \\ &= \frac{1}{\tau\sqrt{2\pi}}\int_0^{\tilde{t}} \exp\left(-\frac{1}{\sqrt{2\pi}}\frac{1}{\tilde{\xi}_\infty(\tilde{k})}\frac{\tilde{t}'}{\tau}\right)\,\mathrm{d}\tilde{t}' \,.\end{aligned}$$

Transforming back to real space, the integrand becomes a Gaussian in $\tilde{x}$, and we obtain the full space-time evolution of the ridge,

$$\tilde{\xi}(\tilde{x},\tilde{t}) = \frac{1}{2}\int_0^{\tilde{t}} \frac{\exp\left(-\frac{\tilde{x}^2\tau}{4\sigma\tilde{t}'}-\frac{\tilde{t}'}{\tau s}\right)}{\sqrt{\pi\sigma\tau\,\tilde{t}'}}\,\mathrm{d}\tilde{t}' \,. \quad (47)$$

The accuracy of this analytical result is confirmed in Fig. 12. The upper panel compares the predicted dynamics of tip growth, Eq. (47) for $\tilde{x}=0$, with direct numerical simulations for several effective substrate viscosities τ; the two are in excellent agreement over the entire build-up, and the corresponding half-value times $\tilde{\tau}_{1/2}$ are marked by diamond symbols. The lower panel shows these half-value times as a function of τ, again comparing the simulation (diamonds) with the analytical estimate of Eq. (40) (dashed line), and confirms the predicted linear scaling across the full range of investigated viscosities.

References

[1] Gennes, P.-G.: Wetting: Statics and dynamics. Rev. Mod. Phys. **57**, 827–863 (1985) https://doi.org/10.1103/RevModPhys.57.827

[2] Bonn, D., Eggers, J., Indekeu, J., Meunier, J., Rolley, E.: Wetting and spreading. Rev. Mod. Phys. **81**, 739–805 (2009) https://doi.org/10.1103/RevModPhys.81.739

[3] Snoeijer, J.H., Andreotti, B.: Moving contact lines: Scales, regimes, and dynamical transitions. Annu. Rev. Fluid Mech. **45**, 269–292 (2013) https://doi.org/10.1146/annurev-fluid-011212-140734

[4] Ruschak, K.J.: Coating flows. Annu. Rev. Fluid Mech. **17**, 65–89 (1985) https://doi.org/10.1146/annurev.fl.17.010185.000433

[5] Snoeijer, J.H., Andreotti, B., Delon, G., Fermigier, M.: Relaxation of a dewetting contact line. Part 1. A full-scale hydrodynamic calculation. J. Fluid Mech. **579**, 63–83 (2007) https://doi.org/10.1017/S0022112007005216

[6] Delon, G., Fermigier, M., Snoeijer, J.H., Andreotti, B.: Relaxation of a dewetting contact line. Part 2. Experiments. J. Fluid Mech. **604**, 55–75 (2008) https://doi.org/10.1017/S0022112008000979

[7] Snoeijer, J.H., Ziegler, J., Andreotti, B., Fermigier, M., Eggers, J.: Thick films of viscous fluid coating a plate withdrawn from a liquid reservoir. Phys. Rev. Lett. **100**, 244502 (2008) https://doi.org/10.1103/PhysRevLett.100.244502

[8] Gao, P., Li, L., Feng, J.J., Ding, H., Lu, X.-Y.: Film deposition and transition on a partially wetting plate in dip coating. J. Fluid Mech. **791**, 358–383 (2016) https://doi.org/10.1017/jfm.2016.64

[9] Dey, M., Doumenc, F., Guerrier, B.: Numerical simulation of dip-coating in the evaporative regime. Eur. Phys. J. E **39**, 19 (2016) https://doi.org/10.1140/epje/i2016-16019-4

[10] Rio, E., Boulogne, F.: Withdrawing a solid from a bath: how much liquid is coated? Adv. Colloid Interfac. **247**, 100–114 (2017) https://doi.org/10.1016/j.cis.2017.01.006

[11] Gans, A., Dressaire, E., Colnet, B., Saingier, G., Bazant, M.Z., Sauret, A.: Dip-coating of suspensions. Soft Matter **15**, 252–261 (2019) https://doi.org/10.1039/c8sm01785a

[12] Tewes, W., Wilczek, M., Gurevich, S.V., Thiele, U.: Self-organised dip-coating patterns of simple, partially wetting, nonvolatile liquids. Phys. Rev. Fluids **4**, 123903 (2019)

https://doi.org/10.1103/PhysRevFluids.4.123903

[13] Champougny, L., Scheid, B., Korobkin, A.A., Rodriguez-Rodriguez, J.: Dip-coating flow in the presence of two immiscible liquids. J. Fluid Mech. **922**, 26 (2021) https://doi.org/10.1017/jfm.2021.541

[14] Landau, L., Levich, B.: Dragging of a liquid by a moving plane. Acta Physicochim. Urs. **17**, 42 (1942) https://doi.org/10.1016/b978-0-08-092523-3.50016-2 . reprinted in [?], p. 141–151

[15] Derjaguin, B.: On the thickness of the liquid film adhering to the walls of a vessel after emptying. Acta Physicochim. Urss **20**, 349–352 (1945) https://doi.org/10.1016/0079-6816(93)90022-n

[16] Wilson, S.D.R.: The drag-out problem in film coating theory. J. Eng. Math. **16**, 209–221 (1982) https://doi.org/10.1007/BF00042717

[17] Quéré, D.: Fluid coating on a fiber. Annu. Rev. Fluid Mech. **31**, 347–384 (1999) https://doi.org/10.1146/annurev.fluid.31.1.347

[18] Blodgett, K.B.: Films built by depositing successive monomolecular layers on a solid surface. J. Am. Chem. Soc. **57**, 1007–1022 (1935) https://doi.org/10.1021/ja01309a011

[19] Gennes, P.G.: Deposition of Langmuir-Blodgett layers. Colloid Polym. Sci. **264**, 463–465 (1986) https://doi.org/10.1007/BF01419552

[20] Spratte, K., Riegler, H.: Steady-state morphology and composition of mixed monomolecular films (Langmuir monolayers) at the air/water interface in the vicinity of the 3-phase line - model-calculations and experiments. Langmuir **10**, 3161–3173 (1994) https://doi.org/10.1021/la00021a045

[21] Li, L.Q., Köpf, M.H., Gurevich, S.V., Friedrich, R., Chi, L.F.: Structure formation by dynamic self-assembly. Small **8**, 488–503 (2012) https://doi.org/10.1002/smll.201101930

[22] Köpf, M.H., Thiele, U.: Emergence of the bifurcation structure of a Langmuir-Blodgett transfer model. Nonlinearity **27**, 2711–2734 (2014) https://doi.org/10.1088/0951-7715/27/11/2711

[23] Greene, J.E.: Tracing the 4000 year history of organic thin films: from monolayers on liquids to multilayers on solids. Appl. Phys. Rev. **2**, 011101 (2015) https://doi.org/10.1063/1.4907770

[24] Teletzke, G.F., Davis, H.T., Scriven, L.E.: Wetting hydrodynamics. Rev. Phys. Appl. (Paris) **23**, 989–1007 (1988) https://doi.org/10.1051/rphysap:01988002306098900

[25] Ziegler, J., Snoeijer, J.H., Eggers, J.: Film transitions of receding contact lines. Eur. Phys. J.-Spec. Top. **166**, 177–180 (2009) https://doi.org/10.1140/epjst/e2009-00902-3

[26] Galvagno, M., Tseluiko, D., Lopez, H., Thiele, U.: Continuous and discontinuous dynamic unbinding transitions in drawn film flow. Phys. Rev. Lett. **112**, 137803 (2014) https://doi.org/10.1103/PhysRevLett.112.137803

[27] Tseluiko, D., Galvagno, M., Thiele, U.: Collapsed heteroclinic snaking near a heteroclinic chain in dragged meniscus problems. Eur. Phys. J. E **37**, 33 (2014) https://doi.org/10.1140/epje/i2014-14033-2

[28] Eggers, J.: Hydrodynamic theory of forced dewetting. Phys. Rev. Lett. **93**, 094502 (2004) https://doi.org/10.1103/PhysRevLett.93.094502

[29] Eggers, J.: Existence of receding and advancing contact lines. Phys. Fluids **17**, 082106 (2005) https://doi.org/10.1063/1.2009007

[30] Chan, T.S., Snoeijer, J.H., Eggers, J.: Theory of the forced wetting transition. Phys. Fluids **24**, 072104 (2012) https://doi.org/10.1063/1.4736531

[31] Bertin, V., Snoeijer, J.H., Raphael, E., Salez, T.: Enhanced dip coating on a soft substrate.

Phys. Rev. Fluids **7**, 102002 (2022) https://doi.org/10.1103/PhysRevFluids.7.L102002

[32] Style, R.W., Jagota, A., Hui, C.Y., Dufresne, E.R.: Elastocapillarity: Surface tension and the mechanics of soft solids. Annu. Rev. Condens. Matter Phys. **8**, 99–118 (2017) https://doi.org/10.1146/annurev-conmatphys-031016-025326

[33] Bico, J., Reyssat, E., Roman, B.: Elastocapillarity: when surface tension deforms elastic solids. Annu. Rev. Fluid Mech. **50**, 629–659 (2018) https://doi.org/10.1146/annurev-fluid-122316-050130

[34] Andreotti, B., Snoeijer, J.H.: Statics and dynamics of soft wetting. Annu. Rev. Fluid Mech. **52**, 285–308 (2020) https://doi.org/10.1146/annurev-fluid-010719-060147

[35] Butt, H.-J., Berger, R., Steffen, W., Vollmer, D., Weber, S.A.L.: Adaptive wetting - adaptation in wetting. Langmuir **34**, 11292–11304 (2018) https://doi.org/10.1021/acs.langmuir.8b01783

[36] Style, R.W., Dufresne, E.R.: Static wetting on deformable substrates, from liquids to soft solids. Soft Matter **8**, 7177–7184 (2012) https://doi.org/10.1039/c2sm25540e

[37] Style, R.W., Hyland, C., Boltyanskiy, R., Wettlaufer, J.S., Dufresne, E.R.: Surface tension and contact with soft elastic solids. Nat. Commun. **4**, 2728 (2013) https://doi.org/10.1038/ncomms3728

[38] Carre, A., Gastel, J.C., Shanahan, M.E.R.: Viscoelastic effects in the spreading of liquids. Nature **379**, 432–434 (1996) https://doi.org/10.1038/379432a0

[39] Karpitschka, S., Das, S., Gorcum, M., Perrin, H., Andreotti, B., Snoeijer, J.H.: Droplets move over viscoelastic substrates by surfing a ridge. Nat. Commun. **6**, 7891 (2015) https://doi.org/10.1038/ncomms8891

[40] Greve, D., Hartmann, S., Thiele, U.: Stick-slip dynamics in the forced wetting of polymer brushes. Soft Matter **19**, 4041–4061 (2023) https://doi.org/10.1039/D3sM00104K

[41] Mokbel, D., Aland, S., Karpitschka, S.: Stick-slip contact line motion on Kelvin-Voigt model substrates. Europhys. Lett. **139**, 33002 (2022) https://doi.org/10.1209/0295-5075/ac6ca6

[42] Skotheim, J.M., Mahadevan, L.: Soft lubrication. Phys. Rev. Lett. **92**, 245509 (2004) https://doi.org/10.1103/PhysRevLett.92.245509

[43] Diekmann, J., Thiele, U.: Mesoscopic hydrodynamic model for spreading, sliding and coarsening compound drops. Phys. Rev. Fluids **10**, 024002 (2025) https://doi.org/10.1103/PhysRevFluids.10.024002

[44] Henkel, C., Snoeijer, J.H., Thiele, U.: Gradient-dynamics model for liquid drops on elastic substrates. Soft Matter **17**, 10359–10375 (2021) https://doi.org/10.1039/D1sM01032H

[45] Thiele, U.: Thin film evolution equations from (evaporating) dewetting liquid layers to epitaxial growth. J. Phys.: Condens. Matter **22**, 084019 (2010) https://doi.org/10.1088/0953-8984/22/8/084019

[46] Oron, A., Davis, S.H., Bankoff, S.G.: Long-scale evolution of thin liquid films. Rev. Mod. Phys. **69**, 931–980 (1997) https://doi.org/10.1103/RevModPhys.69.931

[47] Thiele, U.: Recent advances in and future challenges for mesoscopic hydrodynamic modelling of complex wetting. Colloids Surf. A **553**, 487–495 (2018) https://doi.org/10.1016/j.colsurfa.2018.05.049

[48] Pismen, L.M.: Mesoscopic hydrodynamics of contact line motion. Colloid Surf. A-Physicochem. Eng. Asp. **206**, 11–30 (2002) https://doi.org/10.1016/S0927-7757(02)00059-6

[49] Popescu, M.N., Oshanin, G., Dietrich, S., Cazabat, A.M.: Precursor films in wetting phenomena. J. Phys.: Condens. Matter

24, 243102 (2012) https://doi.org/10.1088/0953-8984/24/24/243102

[50] Johnson, K.L.: Contact Mechanics. Cambridge University Press, Cambridge (1985). https://doi.org/10.1017/CBO9781139171731s

[51] Doedel, E.J., Champneys, A.R., Dercole, F., Fairgrieve, T.F., Kuznetsov, Y.A., Oldeman, B.E., Paffenroth, R.C., Sandstede, B., Wang, X.J., Zhang, C.: AUTO-07p: Continuation and Bifurcation Software for Ordinary Differential Equations. Concordia University, (2007). Concordia University

[52] Diddens, C., Rocha, D.: Bifurcation tracking on moving meshes and with consideration of azimuthal symmetry breaking instabilities. J. Comput. Phys. **518**, 113306 (2024) https://doi.org/10.1016/j.jcp.2024.113306

[53] Heil, M., Hazel, A.L.: Oomph-lib – an object-oriented multi-physics finite-element library. In: Bungartz, H.-J., Schäfer, M. (eds.) Fluid-Structure Interaction: Modelling, Simulation, Optimisation, pp. 19–49. Springer, Berlin, Heidelberg (2006). https://doi.org/10.1007/3-540-34596-5_2

[54] Hazel, A.L., Heil, M.: Oomph-lib online documentation (2006). https://oomph-lib.github.io/oomph-lib Accessed 2025-04-01

[55] Bauer, C., Frink, A., Kreckel, R.: Introduction to the GiNaC framework for symbolic computation within the C++ programming language. J. Symb. Comput. **33**, 1–12 (2002) https://doi.org/10.1006/jsco.2001.0494

[56] Krauskopf, B., Osinga, H.M., Galan-Vioque, J. (eds.): Numerical Continuation Methods for Dynamical Systems. Springer, Dordrecht (2007). https://doi.org/10.1007/978-1-4020-6356-5

[57] Engelnkemper, S., Gurevich, S.V., Uecker, H., Wetzel, D., Thiele, U.: Continuation for thin film hydrodynamics and related scalar problems. In: Gelfgat, A. (ed.) Computational Modeling of Bifurcations and Instabilities in Fluid Mechanics. Computational Methods in Applied Sciences, vol 50, pp. 459–501. Springer, Cham (2019). https://doi.org/10.1007/978-3-319-91494-7_13

[58] Thiele, U., Velarde, M.G., Neuffer, K.: Dewetting: Film rupture by nucleation in the spinodal regime. Phys. Rev. Lett. **87**, 016104 (2001) https://doi.org/10.1103/PhysRevLett.87.016104

[59] Voss, F., Thiele, U.: Chemomechanical motility modes of partially wetting liquid droplets. Phys. Rev. Fluids **10**, 094005 (2025) https://doi.org/10.1103/f3ck-dx5c

[60] Li, Z., Ren, W.: The motion of a thin drop on an elastic sheet. J. Fluid Mech. **1022**, 4 (2025) https://doi.org/10.1017/jfm.2025.10779

[61] Leger, L., Joanny, J.F.: Liquid spreading. Rep. Prog. Phys. **55**, 431–486 (1992) https://doi.org/10.1088/0034-4885/55/4/001

[62] Marmur, A.: Equilibrium contact angles: Theory and measurement. Colloid Surf. A-Physicochem. Eng. Asp. **116**, 55–61 (1996) https://doi.org/10.1016/0927-7757(96)03585-6

[63] Schäffer, E., Wong, P.Z.: Contact line dynamics near the pinning threshold: A capillary rise and fall experiment. Phys. Rev. E **61**, 5257–5277 (2000) https://doi.org/10.1103/physreve.61.5257

[64] Cubaud, T., Fermigier, A.: Advancing contact lines on chemically patterned surfaces. J. Colloid Interface Sci. **269**, 171–177 (2004) https://doi.org/10.1016/j.jcis.2003.08.008

[65] Quéré, D.: Wetting and roughness. Ann. Rev. Mater. Res. **38**, 71–99 (2008) https://doi.org/10.1146/annurev.matsci.38.060407.132434

[66] Savva, N., Kalliadasis, S., Pavliotis, G.A.: Two-dimensional droplet spreading over random topographical substrates. Phys. Rev. Lett. **104**, 084501 (2010) https://doi.org/10.1103/PhysRevLett.104.084501

[67] Robbins, M.O., Joanny, J.F.: Contact angle hysteresis on random surfaces. Europhys. Lett. **3**, 729–735 (1987) https://doi.org/10.1209/0295-5075/3/6/013

[68] Nadkarni, G.D., Garoff, S.: Reproducibility of contact line motion on surfaces exhibiting contact angle hysteresis. Langmuir **10**, 1618–1623 (1994) https://doi.org/10.1021/la00017a049

[69] Schwartz, L.W., Garoff, S.: Contact-angle hysteresis on heterogeneous surfaces. Langmuir **1**, 219–230 (1985) https://doi.org/10.1021/la00062a007

[70] Brandon, S., Marmur, A.: Simulation of contact angle hysteresis on chemically heterogeneous surfaces. J. Colloid Interface Sci. **183**, 351–355 (1996) https://doi.org/10.1006/jcis.1996.0556

[71] Thiele, U., Knobloch, E.: On the depinning of a driven drop on a heterogeneous substrate. New J. Phys. **8**, 313 (2006) https://doi.org/10.1088/1367-2630/8/12/313

[72] Savva, N., Kalliadasis, S.: Two-dimensional droplet spreading over topographical substrates. Phys. Fluids **21**, 092102 (2009) https://doi.org/10.1063/1.3223628

[73] Varagnolo, S., Ferraro, D., Fantinel, P., Pierno, M., Mistura, G., Amati, G., Biferale, L., Sbragaglia, M.: Stick-slip sliding of water drops on chemically heterogeneous surfaces. Phys. Rev. Lett. **111**, 066101 (2013) https://doi.org/10.1103/PhysRevLett.111.066101

[74] Sbragaglia, M., Biferale, L., Amati, G., Varagnolo, S., Ferraro, D., Mistura, G., Pierno, M.: Sliding drops across alternating hydrophobic and hydrophilic stripes. Phys. Rev. E **89**, 012406 (2014) https://doi.org/10.1103/PhysRevE.89.012406

[75] Deegan, R.D.: Pattern formation in drying drops. Phys. Rev. E **61**, 475–485 (2000) https://doi.org/10.1103/PhysRevE.61.475

[76] Bodiguel, H., Doumenc, F., Guerrier, B.: Stick-slip patterning at low capillary numbers for an evaporating colloidal suspension. Langmuir **26**, 10758–10763 (2010) https://doi.org/10.1021/la100547j

[77] Han, W., Lin, Z.: Learning from "Coffee Rings": Ordered structures enabled by controlled evaporative self-assembly. Angew. Chem. Int. Ed. **51**, 1534–1546 (2012) https://doi.org/10.1002/anie.201104454

[78] Fraštia, L., Archer, A.J., Thiele, U.: Modelling the formation of structured deposits at receding contact lines of evaporating solutions and suspensions. Soft Matter **8**, 11363–11386 (2012) https://doi.org/10.1039/C2SM26574E

[79] Larson, R.G.: Transport and deposition patterns in drying sessile droplets. Aiche J. **60**, 1538–1571 (2014) https://doi.org/10.1002/aic.14338

[80] Thiele, U.: Patterned deposition at moving contact lines. Adv. Colloid Interface Sci. **206**, 399–413 (2014) https://doi.org/10.1016/j.cis.2013.11.002

[81] Jabal, M.A., Egbaria, A., Zigelman, A., Thiele, U., Manor, O.: Connecting monotonic and oscillatory motions of the meniscus of a volatile polymer solution to the transport of polymer coils and deposit morphology. Langmuir **34**, 11784–11794 (2018) https://doi.org/10.1021/acs.langmuir.8b02268

[82] Wan, L.S., Meng, X.L., Yang, Y.F., Tian, J., Xu, Z.K.: Thermo-responsive stick-slip behavior of advancing water contact angle on the surfaces of poly(N-isopropylacrylamide)-grafted polypropylene membranes. Sci. China Chem. **53**, 183–189 (2010) https://doi.org/10.1007/s11426-010-0004-4

[83] Schubotz, S., Honnigfort, C., Nazari, S., Fery, A., Sommer, J.-U., Uhlmann, P., Braunschweig, B., Auernhammer, G.K.: Memory effects in polymer brushes showing co-nonsolvency effects. Adv. Colloid Interface Sci. **294**, 102442 (2021) https://doi.org/10.1016/j.cis.2021.102442

[84] Kajiya, T., Daerr, A., Narita, T., Royon, L., Lequeux, F., Limat, L.: Advancing liquid contact line on visco-elastic gel substrates: Stick-slip vs. continuous motions. Soft Matter **9**, 454–461 (2013) https://doi.org/10.1039/c2sm26714d

[85] Kajiya, T., Brunet, P., Royon, L., Daerr, A., Receveur, M., Limat, L.: A liquid contact line receding on a soft gel surface: dip-coating geometry investigation. Soft Matter **10**, 8888–8895 (2014) https://doi.org/10.1039/c4sm01609b

[86] Park, S.J., Bostwick, J.B., De Andrade, V., Je, J.H.: Self-spreading of the wetting ridge during stick-slip on a viscoelastic surface. Soft Matter **13**, 8331–8336 (2017) https://doi.org/10.1039/c7sm01408b

[87] Gorcum, M., Andreotti, B., Snoeijer, J.H., Karpitschka, S.: Dynamic solid surface tension causes droplet pinning and depinning. Phys. Rev. Lett. **121**, 208003 (2018) https://doi.org/10.1103/PhysRevLett.121.208003

[88] Gilcreest, V.P., Carroll, W.M., Rochev, Y.A., Blute, I., Dawson, K.A., Gorelov, A.V.: Thermoresponsive poly(n-isopropylacrylamide) copolymers: Contact angles and surface energies of polymer films. Langmuir **20**, 10138–10145 (2004) https://doi.org/10.1021/la0487996

[89] Leong, F.Y., Le, D.-V.: Droplet dynamics on viscoelastic soft substrate: toward coalescence control. Phys. Fluids **32**, 062102 (2020) https://doi.org/10.1063/5.0011151

[90] Hartmann, S., Diekmann, J., Greve, D., Thiele, U.: Drops on polymer brushes: advances in thin-film modeling of adaptive substrates. Langmuir **40**, 4001–4021 (2024) https://doi.org/10.1021/acs.langmuir.3c03313

[91] Extrand, C.W.: Modeling of ultralyophobicity: suspension of liquid drops by a single asperity. Langmuir **21**, 10370–10374 (2005) https://doi.org/10.1021/la0513050

[92] Tóth, T., Ferraro, D., Chiarello, E., Pierno, M., Mistura, G., Bissacco, G., Semprebon, C.: Suspension of water droplets on individual pillars. Langmuir **27**, 4742–4748 (2011) https://doi.org/10.1021/la2001249

[93] Tsoumpas, Y., Dehaeck, S., Galvagno, M., Rednikov, A., Ottevaere, H., Thiele, U., Colinet, P.: Non equilibrium Gibbs' criterion for completely wetting volatile liquids. Langmuir **30**, 11847–11852 (2014) https://doi.org/10.1021/la502708f http://arxiv.org/abs/1410.6783